

Quality open source mesh generation for cardiovascular flow simulations

E. Marchandise, P. Crosetto, C. Geuzaine, J.-F. Remacle and E. Sauvage

Abstract We present efficient algorithms for generating quality tetrahedral meshes for cardiovascular blood flow simulations starting from low quality triangulations obtained from the segmentation of patient specific medical images. The suite of algorithms that are presented in this paper have been implemented in the open-source mesh generator Gmsh [23]. This includes a high quality remeshing algorithm based on a finite element conformal parametrization and a volume meshing algorithm with a boundary layer generation technique. In the result section, the influence of tetrahedral mesh quality and mesh algorithm for cardiovascular flow simulations is discussed.

Emilie Marchandise
Université catholique de Louvain, institute of Mechanics, Materials and Civil Engineering (iMMC), Belgium, e-mail: emilie.marchandise@uclouvain.be

Emilie Sauvage
Université catholique de Louvain, institute of Mechanics, Materials and Civil Engineering (iMMC), Belgium, e-mail: emilie.sauvage@uclouvain.be

Paolo Crosetto
Ecole Polytechnique Fdrale de Lausanne (EPFL), Switzerland, e-mail: paolo.crosetto@epfl.ch

Christophe Geuzaine
Université de Liège, Department of Electrical Engineering and Computer Science, Liège, Belgium
e-mail: cgeuzaine@ulg.ac.be

Jean-Francois Remacle
Université catholique de Louvain, institute of Mechanics, Materials and Civil Engineering (iMMC), Belgium, e-mail: jean-francois.remacle@uclouvain.be

1 Introduction

Blood flow dynamics and arterial wall mechanics are thought to be an important factor in the pathogenesis and treatment of cardiovascular diseases. A number of specific hemodynamic and vascular mechanic factors - notably wall shear stress (WSS), pressure and mural stress, flow rate, and residence time - have been implicated in aneurysm growth and rupture [11, 42] or in the pathogenesis of atherosclerosis [28]. Judicious control of these hemodynamic factors may also govern the outcomes of vascular therapies [24, 25]. Blood flow simulations with either rigid or compliant walls provide a viable option for understanding the complex nature of blood flow and arterial wall mechanics and for obtaining those relevant quantities. Those numerical computations require meshes describing the patient-specific three-dimensional cardiovascular geometry.

The quality of the meshes is of great importance since it impacts both on the accuracy and the efficiency of the numerical method [43, 7]. For example, it is well known that for finite element computations, the discretization error in the finite element solution increases when the angles of the mesh elements become too large [4], and that the condition number of the elementary matrix increases with small angles [20] which hinders the numerical convergence.

Two important elements have to be taken into account in order to generate a high quality tetrahedral mesh for cardiovascular simulations from medical images: (i) the quality of the triangular surface mesh, (ii) the capability to generate boundary layers meshes.

Most of the current imaging techniques allow to extract only the inner wall of the arteries, called also lumen surface. The outcome of the segmentation procedure is then a triangulation of the lumen surface. Those triangulations are however not suited for subsequent numerical simulations since they are generally oversampled and of very low quality (with poorly shaped and distorted triangles). It is then desirable to modify the initial surface mesh to generate a new surface mesh with nearly equilateral triangles of given triangle density (e.g. density based on the vessel radius). There exists mainly two approaches for surface remeshing: mesh adaptation strategies [26, 9, 45] and meshing techniques that rely on a suitable surface parametrization [10, 30]. The mesh adaptation strategies belong to the direct meshing methods and use local mesh modifications in order both to improve the quality of the input surface mesh and to adapt the mesh to a given mesh size criterion. The parametrization techniques belong to the indirect meshing approach. The initial 3D surface mesh is first parametrized onto a 2D planar surface mesh; the initial surface can then be remeshed using any 2D mesh generation procedure with any given mesh size field by subsequently mapping the new mesh back to the original surface. In this paper we first propose an efficient approach based on parametrization for recovering a high quality surface mesh from a low quality input triangulation. The parametrization technique is based on discrete finite element conformal maps [38, 32] and the density of the new mesh can be for example adapted to the vessel radius or the discrete mean curvature (for an example of a curvature adapted mesh of an aneurysm, see [39]).

The proposed quality surface remeshing algorithm is of high importance for subsequent three-dimensional blood flow simulations. Indeed, the lumen surface triangulation is most of the time taken as input for the tetrahedral mesh generator (e.g. Delaunay, Frontal), which retains the remeshed surface as the boundary of the resulting tetrahedral mesh. Hence if the surface mesh contains low quality triangles with small angles, the resulting tetrahedral mesh might contain some degenerate tetrahedra with small volumes and small dihedral angles. Those degenerate triangles may lead to large interpolation errors, and have a negative effect on the convergence rate of the solution procedure. The worst impact results in an unresolvable system of equations.

In the context of cardiovascular flow simulations, another important point concerns the generation of a mesh boundary layer that is able to capture at the vicinity of the wall derived quantities of clinical interest. While many authors still use fully unstructured isotropic tetrahedral meshes, those meshes are not efficient in terms of computational time. Indeed, they require a huge number of elements in order to have sufficiently small elements near the wall to resolve the boundary layer and to be able to capture accurately derived quantities such as WSS. Moreover, some authors have reported that those meshes can produce spurious fluctuations for the WSS [?, 40]. Boundary layer meshes permit to capture those derived quantities accurately while keeping for efficiency purposes a reasonable number of mesh elements. Those meshes can be built with an advancing layer method [21, 14, 27] that extrudes the lumen surface mesh in the inward direction. The extruded prisms are then subsequently split into tetrahedra and the remaining of the lumen volume filled with tetrahedra. For blood flow simulations with compliant walls, one has to build also the vascular wall. Using the presented mesh boundary layer technique, the vascular wall can be built by extruding the lumen surface mesh in the outward direction with a given wall thickness.

Section 2 presents two meshing algorithms for cardiovascular simulations. The first algorithm is a surface remeshing method based on a finite element conformal parametrization and the second is volume meshing algorithm with a mesh boundary layer generation technique. Section 3 shows mesh quality statistics for cardiovascular meshes generated with the presented algorithms. Finally simulation results are given in section 4 that show the impact of tetrahedral mesh quality for cardiovascular flow simulations.

2 Methods

In this section, we present the algorithms included in the open source pipeline for the generation of high quality meshes for cardiovascular blood flow simulations. Our proposed meshing pipeline consists mainly of two steps, which are described in the following subsections: (i) From a given triangulation of the lumen surface, use finite element conformal parametrizations to create a new surface mesh with a higher quality and a computational mesh size field (ii) extrude the lumen surface mesh

outward and inward in order to build the vascular wall and the viscous boundary layer mesh for the blood flow.

The last meshing step involves the use of a tetrahedral mesh generator to mesh the two extruded volumes as well as the remaining volume of the lumen. All the presented algorithms are implemented in the open-source mesh generator Gmsh [23] and examples can be found on the Gmsh wiki¹.

2.1 Surface remeshing with finite element conformal maps

The remeshing technique we present is based on a least square conformal parametrization of a given triangulated surface S . Parametrizing a surface S is defining a map $\mathbf{u}(\mathbf{x})$ (see Fig. 1):

$$\mathbf{x} \in S \subset \mathbb{R}^3 \mapsto \mathbf{u}(\mathbf{x}) \in S' \subset \mathbb{R}^2 \quad (1)$$

that transforms continuously a 3D surface S into a surface S' embedded in \mathbb{R}^2 that has a well known parametrization. As shown in [38] and [33] such a parametrization exists if the two surfaces S and S' have the same topology, that is have zero genus and have at least one boundary. Moreover, as we have shown in [38, 33] the geometrical aspect ratio should be moderate to prevent the numerical issue of indistinguishable coordinates, which is often not the case for vascular geometries. Our remeshing algorithm is fully automatic, it detects if the topology is wrong and/or if the aspect ratio is too high and if necessary calls a multilevel partitioning algorithm to create different patches of correct topology and moderate aspect ratio [32]. Those patches are then subsequently remeshed with a finite element least square conformal map.

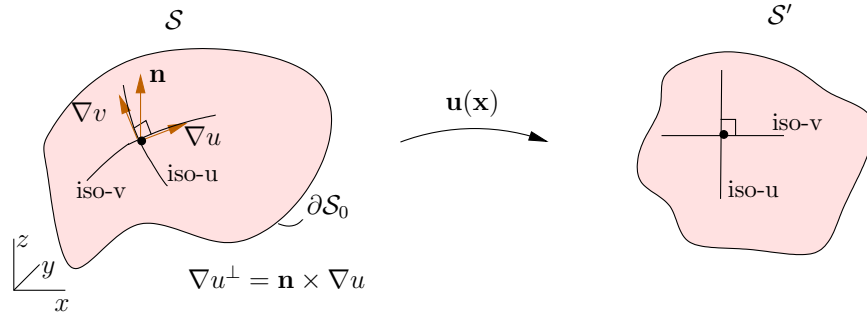


Fig. 1 Definitions for a conformal mapping $\mathbf{u}(\mathbf{x})$ of a 3D surface S with one boundary ∂S_0 . ∇u^\perp denotes the counterclockwise 90° rotation of the gradient ∇u for the 3D surface.

¹ Gmsh's wiki: <https://geuz.org/trac/gmsh> (username: gmsh, password: gmsh)

The least square conformal map as introduced by Levy et al. [31] asks that the gradient of u and the gradient of v be as orthogonal as possible in the parametrization and have the same norm. This can be seen as an approximation of the Cauchy-Riemann equations. For a piecewise linear mapping, the least square conformal map can be obtained by minimizing the conformal energy:

$$E_{\text{LSCM}}(\mathbf{u}) = \int_S \frac{1}{2} |\nabla u^\perp - \nabla v|^2 ds, \quad (2)$$

where $^\perp$ denotes a counterclockwise 90° rotation in S . For a 3D surface with normal vector \mathbf{n} , the counterclockwise rotation of the gradient can be written as: $\nabla u^\perp = \mathbf{n} \times \nabla u$ (see Fig. 1). Equation (2) can be simplified and rewritten as follows:

$$\begin{aligned} E_{\text{LSCM}}(\mathbf{u}) &= \int_S \frac{1}{2} \left(\nabla u^\perp \cdot \nabla u^\perp + \nabla v \cdot \nabla v - 2 \nabla u^\perp \cdot \nabla v \right) ds, \\ &= \int_S \frac{1}{2} \left(\nabla u \cdot \nabla u + \nabla v \cdot \nabla v - 2 (\mathbf{n} \times \nabla u) \cdot \nabla v \right) ds. \end{aligned} \quad (3)$$

Recalling that a “dot” and a “cross” can be interchanged without changing the result, we have:

$$E_{\text{LSCM}}(\mathbf{u}) = \int_S \frac{1}{2} \left(\nabla u \cdot \nabla u + \nabla v \cdot \nabla v - 2 \mathbf{n} \cdot (\nabla u \times \nabla v) \right) ds. \quad (4)$$

We now derive the finite element formulation of the quadratic minimization problem (2):

$$\min_{\mathbf{u} \in \mathbf{U}(S)} E_{\text{LSCM}}(\mathbf{u}), \quad \text{with } \mathbf{U}(S) = \{\mathbf{u} \in H^1(S), \mathbf{u} = \mathbf{u}_D(\mathbf{x}) \text{ on } \partial S_0\}, \quad (5)$$

where ∂S_0 is one of the boundaries of S . We assume the following finite expansions for $\mathbf{u} = \{u, v\}$:

$$\mathbf{u}_h(\mathbf{x}) = \sum_{i \in I} \mathbf{u}_i \phi_i(\mathbf{x}) + \sum_{i \in J} \mathbf{u}_D(\mathbf{x}_i) \phi_i(\mathbf{x}) \quad (6)$$

where I denotes the set of nodes of S that do not belong to the Dirichlet boundary, J denotes the set of nodes of S that belong to the Dirichlet boundary and where ϕ_i are the nodal shape functions associated with the nodes of the mesh. We assume here that nodal shape function ϕ_i is equal to 1 on vertex \mathbf{x}_i and 0 on any other vertex: $\phi_i(\mathbf{x}_j) = \delta_{ij}$.

Thanks to (6) the functional E_{LSCM} defining the energy of the least square conformal map Eq. (3) can be rewritten as

$$\begin{aligned}
E_{\text{LSCM}}(\mathbf{u}_1, \dots, \mathbf{u}_N) &= \frac{1}{2} \sum_{i \in I} \sum_{j \in I} u_i u_j \int_S \nabla \phi_i \cdot \nabla \phi_j ds + \sum_{i \in I} \sum_{j \in J} u_i u_D(\mathbf{x}_j) \int_S \nabla \phi_i \cdot \nabla \phi_j ds + \\
&\quad \frac{1}{2} \sum_{i \in I} \sum_{j \in I} v_i v_j \int_S \nabla \phi_i \cdot \nabla \phi_j ds + \sum_{i \in I} \sum_{j \in J} v_i v_D(\mathbf{x}_j) \int_S \nabla \phi_i \cdot \nabla \phi_j ds + \\
&\quad \sum_{i \in I} \sum_{j \in J} u_D(\mathbf{x}_i) u_D(\mathbf{x}_j) \int_S \nabla \phi_i \cdot \nabla \phi_j ds + \sum_{i \in I} \sum_{j \in J} v_D(\mathbf{x}_i) v_D(\mathbf{x}_j) \int_S \nabla \phi_i \cdot \nabla \phi_j ds - \\
&\quad \sum_{i \in I} \sum_{j \in J} u_i v_j \int_S \mathbf{n} \cdot (\nabla \phi_i \times \nabla \phi_j) ds - \sum_{i \in I} \sum_{j \in J} u_D(\mathbf{x}_i) v_j \int_S \mathbf{n} \cdot (\nabla \phi_i \times \nabla \phi_j) ds - \\
&\quad \sum_{i \in I} \sum_{j \in J} u_i v_D(\mathbf{x}_i) \int_S \mathbf{n} \cdot (\nabla \phi_i \times \nabla \phi_j) ds - \sum_{i \in I} \sum_{j \in J} u_D(\mathbf{x}_i) v_D(\mathbf{x}_i) \int_S \mathbf{n} \cdot (\nabla \phi_i \times \nabla \phi_j) ds.
\end{aligned} \tag{7}$$

In order to minimize E_{LSCM} , we can simply cancel the derivative of E_{LSCM} with respect to u_k

$$\begin{aligned}
\frac{\partial E_{\text{LSCM}}}{\partial u_k} &= \sum_{j \in I} u_j \underbrace{\int_S \nabla \phi_k \cdot \nabla \phi_j ds}_{A_{kj}} + \sum_{j \in J} u_D(\mathbf{x}_j) \underbrace{\int_S \nabla \phi_k \cdot \nabla \phi_j ds}_{A_{kj}} - \\
&\quad \sum_{j \in I} v_j \underbrace{\int_S \mathbf{n} \cdot (\nabla \phi_k \times \nabla \phi_j) ds}_{C_{kj}} - \sum_{j \in I} v_D(\mathbf{x}_j) \underbrace{\int_S \mathbf{n} \cdot (\nabla \phi_k \times \nabla \phi_j) ds}_{C_{kj}} \\
&= 0, \quad \forall k \in I.
\end{aligned} \tag{8}$$

The same can be done for the derivative with respect to v_k .

The combination of the equations (8) for the u_k and v_k derivatives gives us a linear system of $2I$ equations that can be written as follows:

$$\underbrace{\begin{pmatrix} \mathbf{A} & -\mathbf{C} \\ -\mathbf{C}^T & \mathbf{A} \end{pmatrix}}_{\mathbf{L}_C} \begin{pmatrix} U \\ V \end{pmatrix} = \begin{pmatrix} \mathbf{0} \\ \mathbf{0} \end{pmatrix}, \tag{9}$$

where \mathbf{A} is a symmetric positive definite matrix and \mathbf{C} is an antisymmetric matrix that are both built by assembling the elementary matrices A_{kj} and C_{kj} , and the vectors U and V denote respectively the vector of unknowns u_k and v_k . The resulting matrix \mathbf{L}_C is then symmetric definite positive such that the linear system $\mathbf{L}_C \mathbf{U} = \mathbf{0}$ can be efficiently solved using a direct sparse symmetric-positive-definite solver such as TAUCS².

It is necessary to impose appropriate boundary conditions to guarantee that the discrete minimization problem has a unique solution and that this unique solution defines a one-to-one mapping (and hence avoids the degenerate solution $\mathbf{u} = \text{constant}$). For least square conformal maps, the mapping (9) has full rank only

² <http://www.tau.ac.il/~stoledo/taucs/>

when the number of pinned vertices is greater or equal to 2 [31]. Pinning down two vertices will set the translation, rotation and scale of the solution when solving the linear system $\mathbf{L}_C \mathbf{U} = \mathbf{0}$ and will lead to what is called a free-boundary parametrization. It was independently found by the authors of the LSCM [31] and the DCP [1] that picking two boundary vertices the farthest from each other seems to give good results in general.

Fig. 2 shows the presented surface remeshing procedure applied to part for an aneurysm triangulation. For this example, the chosen mesh size field is a constant.

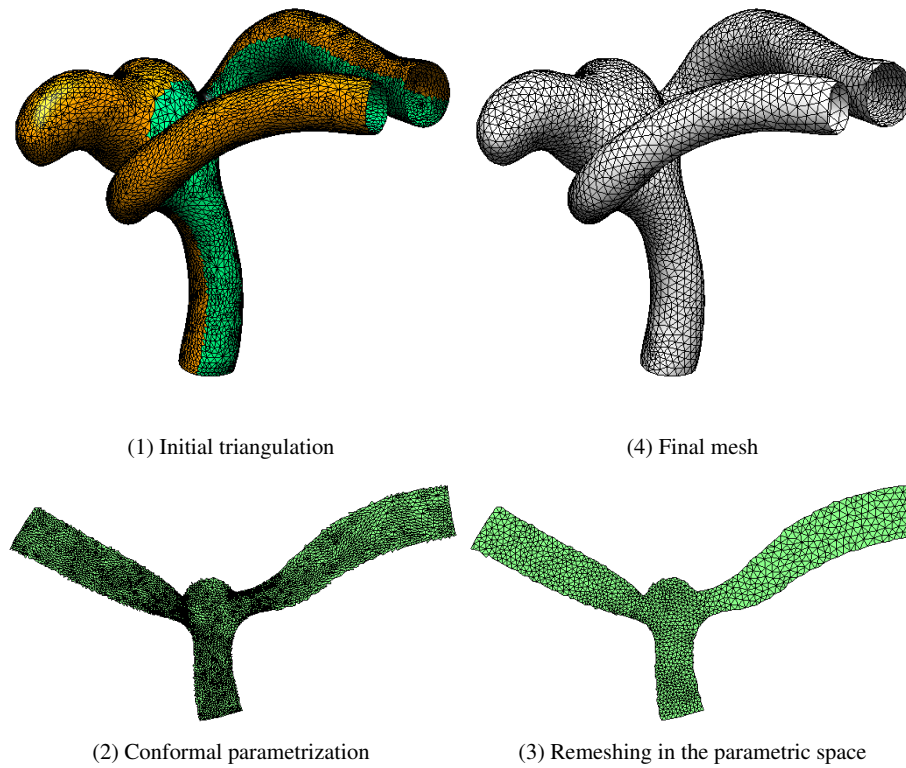


Fig. 2 Illustration of the presented surface remeshing procedure. (1) We start from an initial triangulation that is automatically split into a minimal number of patches (green and orange patch in this case) [33, 32]. (2) Next we compute for each patch the conformal map, and (3) remesh the patch in the parametric space using standard 2D mesh generators. The final mesh is shown in (4).

2.2 Volume meshes with boundary layers

We have implemented an advancing layer method [21, 14, 27] for the generation of boundary layers. The method starts from a surface mesh on which a boundary layer must be grown. From each surface node a direction is picked for placing the nodes of the boundary layer mesh. The direction is either computed using an estimate to the surface normal at the node using Gouraud shading, or specified directly as a three-dimensional vector field—obtained e.g. as the solution of a partial differential equation. The nodes are connected to form layers of prisms that are subsequently subdivided into tetrahedra. Care is taken to produce elements of acceptable shape at sharp corners and to prevent element overlap in regions of tight corners. Those boundary layer meshes are attractive since they present high aspect ratio, orthogonal and possibly graded elements at the wall.

As explained in the introduction, for cardiovascular simulations, there is a double necessity for boundary layer meshes: one for the viscous boundary layer mesh and one for the arterial wall of given thickness. Those boundary layer meshes can be built by extruding outward and inward the lumen surface. Next a three-dimensional Delaunay mesh generator is called to fill the remaining of the lumen volume with isotropic tetrahedra. Figure 3 shows such an example of volume mesh with boundary layers that is well suited for blood flow simulations in compliant vessels.

It should be noted however that for realistic blood flow simulations, the thickness of the viscous boundary layer mesh and the mesh resolution for the inner tetrahedra are often unknown prior to the computation. An effective approach to overcome this difficulty is to start from the pre-defined boundary layer meshes as depicted in Fig. 3 and to apply an adaptive procedure [13, 41, 40] where the distribution of the spatial discretization errors are estimated and controlled by modifying the mesh resolution. For example, in the case of unsteady blood flow simulations, one could rely the adaptation of the mesh size field on an Hessian strategy [29] of the average flow speed over one cardiac cycles [41, 40].

3 High quality meshes

The aim of the mesh generation algorithms described in this paper is to build a mesh made of triangles and tetrahedra that have controlled element sizes and shapes.

As in this work the initial triangulations are remeshed with a given isotropic mesh size field $h(\mathbf{x})$, the quality of remeshed surfaces can be evaluated by computing the aspect ratio of every mesh triangle κ as follows [23]:

$$\gamma_{\kappa} = \alpha \frac{\text{inscribed radius}}{\text{circumscribed radius}} = 4 \frac{\sin \hat{a} \sin \hat{b} \sin \hat{c}}{\sin \hat{a} + \sin \hat{b} + \sin \hat{c}}, \quad (10)$$

$\hat{a}, \hat{b}, \hat{c}$ being the three inner angles of the triangle. With this definition, the equilateral triangle has $\gamma_{\kappa} = 1$ and degenerated (zero surface) triangles have $\gamma_{\kappa} = 0$.

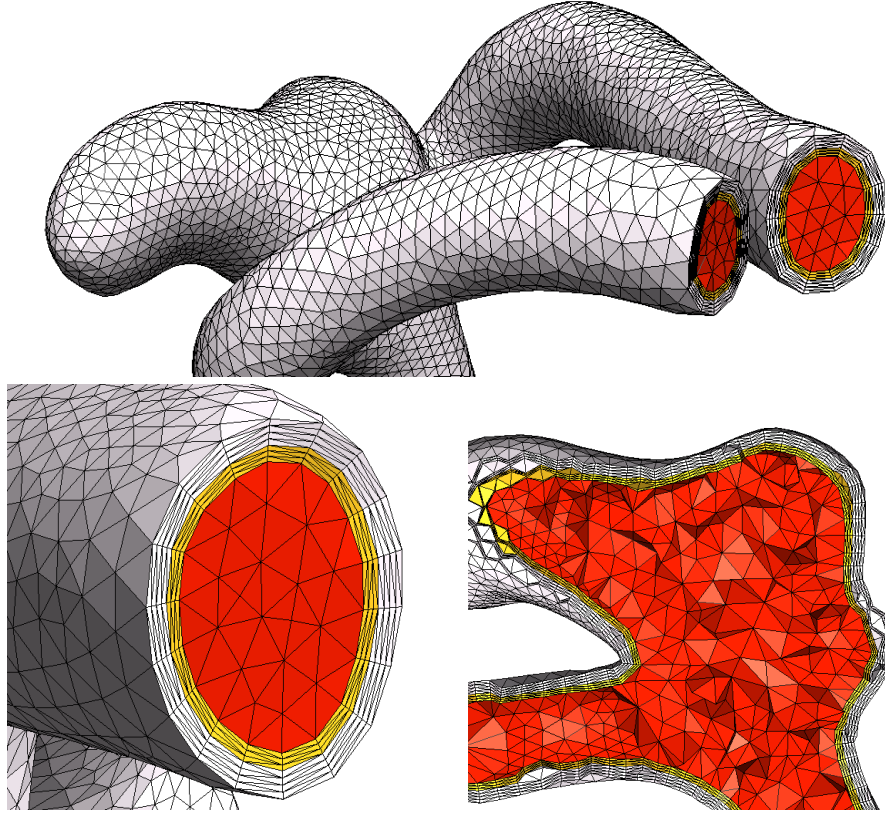


Fig. 3 Magnified views of the boundary layer volume mesh of an aneurysm. The white volume is a boundary layer mesh of the arterial wall, and the red and yellow volumes represent the arterial lumen. The yellow volume is the viscous CFD boundary layer mesh that is built in order to capture accurately the wall shear stresses during the blood flow simulations and the yellow volume is the remaining of the lumen volume that is filled with isotropic tetrahedra.

In order to measure the quality of the isotropic tetrahedral elements, we define another quality measure γ_τ based also on the radius ratio of the mesh element (tetrahedron) [23, 22]:

$$\gamma_\tau = \frac{6\sqrt{6}V_\tau}{S_F^{sum} L_E^{max}},$$

V_τ being the volume of the tetrahedron τ , S_F^{sum} being the sum of the areas of the 4 faces of the tetrahedron, and L_E^{max} being the maximum edge length of the 6 edges of the tetrahedron. This γ_τ quality measure lies in the interval $[0, 1]$, an element with $\gamma_\tau = 0$ being a sliver (zero volume).

In this section, we analyze the quality of the the lumen triangulations obtained with our remeshing algorithm based on finite element conformal maps. The quality of the volume meshes used for the simulations will be presented in the next section.

Figure 4 shows two different steps in the parametrization-based remeshing algorithm of an initial triangulation of an iliac artery bifurcation. First the initial mesh is cut into different patches using the multiscale Laplacian partitioning method described in [33] (Fig. 4a). Next, each mesh partition (orange and green) is parametrized onto a surface in \mathbb{R}^2 with a specific mapping algorithm (Fig. 4bc). We show two different mappings: a Laplacian harmonic map onto a unit disk (Fig. 4b) and the presented conformal map with open boundaries (Fig. 4c). As can be seen, the conformal mapping is much less distorted.

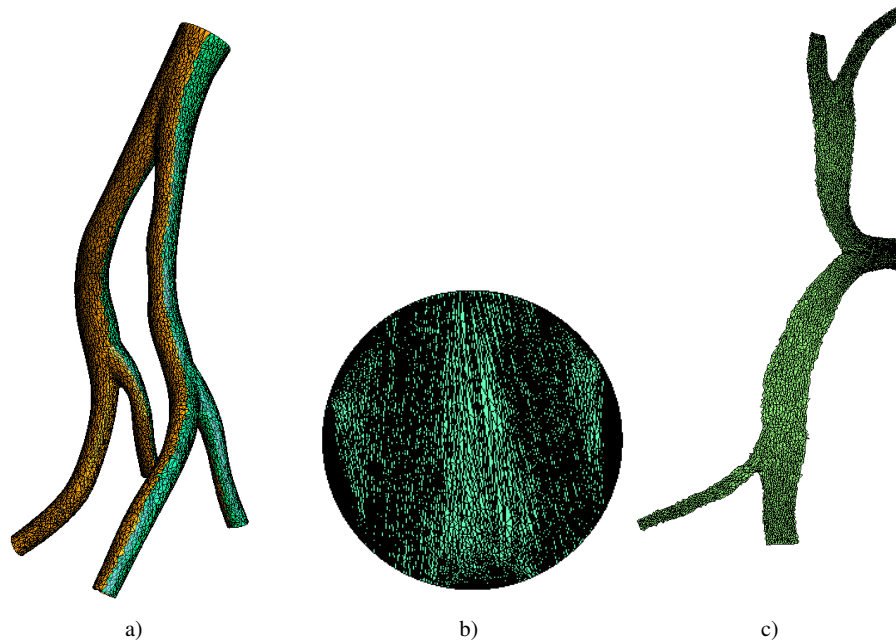


Fig. 4 Remeshing of an iliac bifurcation. The initial mesh is first split into two parts using the multiscale Laplacian partitioning method described in [33] (a). Each of those two parts is then mapped in the parametric space by computing a Laplacian harmonic map onto a unit disk (b) and the presented conformal map with open boundaries (c).

After the mapping has been computed, the parametrized surface is remeshed using a 2D mesh generation algorithm and the new triangulation is then mapped back to the original surface. Figure 5 shows part of the remeshed iliac bifurcation for both the harmonic mapping and the conformal map.

Figure 6 presents the quality histogram for the surface remeshing of the iliac artery. The presented remeshing algorithm based on finite element conformal maps

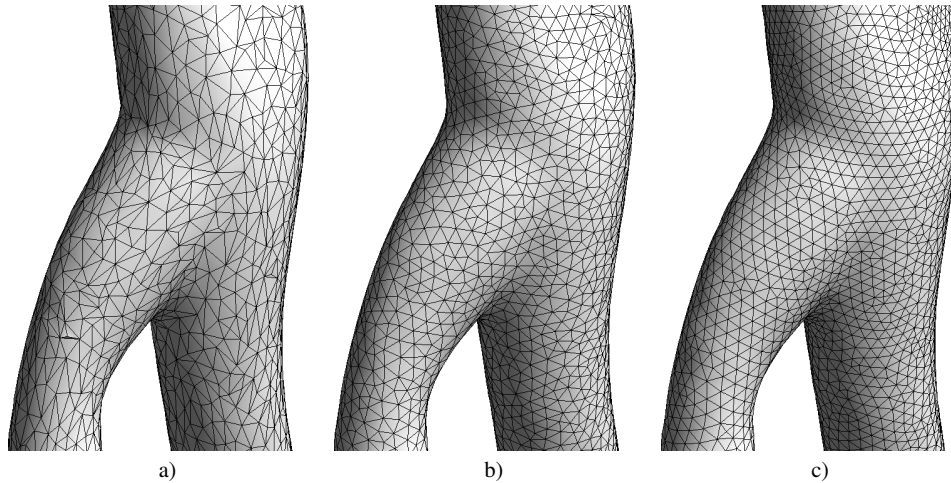


Fig. 5 Remeshing of an iliac bifurcation: a) part of the initial STL triangulation, b) remeshed geometry with the harmonic mapping using the MeshAdapt meshing algorithm, c) remeshed geometry with the presented conformal mapping using a frontal 2D meshing algorithm.

is compared with different surface remeshing techniques: two direct remeshing techniques based respectively on the harmonic mapping [17, 38] and the convex combination map of Floater [18]) and one direct remeshing algorithm based on mesh adaptations (implemented in VMTK [3, 2]). As can be seen in Fig. 4, the harmonic map (and also the convex combination map) is a parametrization with fixed boundaries mapped on a unit circle in contrast with the conformal mapping which is a mapping with open boundaries. The quality histograms of Fig 6 show that the remeshing procedure based on conformal maps renders the highest quality mapping and has less small elements than the two other parametrization-based remeshing methods have. Furthermore, it performs as well as the direct remeshing algorithm of VMTK. Our surface remeshing algorithm is however more robust since it allows to remesh any kind of surface. For example, VMTK was not able to remesh the skull and pelvic surfaces that we remeshed in [32] using our parametrization-based techniques.

An important element in the surface remeshing algorithm is the choice of the planar mesh generator to remesh the parametrized surface (see Fig. 2(2) and 2(3)). In table 1, we compare the quality of the iliac surface meshes using three different planar mesh generators implemented in Gmsh: a Frontal-Delaunay algorithm [37], a planar Delaunay algorithm [22] and an algorithm based on local mesh adaptation (called MeshAdapt, see [23] for more details). Table 1 shows clearly that the best planar mesh generator for the conformal mapping is the Gmsh's Frontal-Delaunay algorithm. This is not a surprise: frontal techniques tend to produce meshes that are close to quadrilateral. Yet, those techniques like it best when the domain that has to be meshed is equipped with a metric that conserves angles, i.e. when the mapping is conformal. The use of conformal mapping helps therefore to obtain better results from the mesh generator, enabling us to produce high quality meshes.

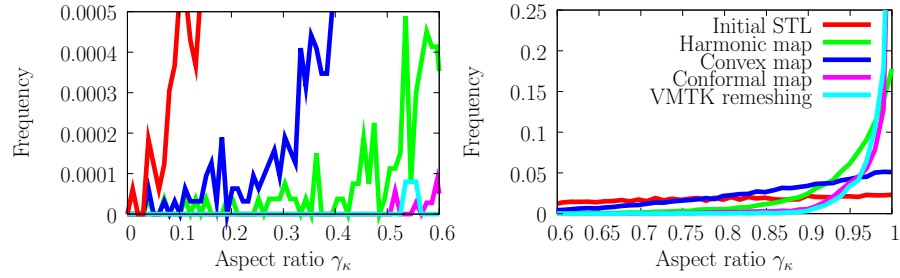


Fig. 6 Quality histogram for the remeshing of an iliac bifurcation and comparison of our remeshing method with other remeshing techniques based on parametrization. The left figure shows a zoom for range of small aspect ratio $\gamma_\kappa \in [0 : 0.6]$ and the right figure the range of high aspect ratio $\gamma_\kappa \in [0.6 : 1]$.

Mesh generator	Surface quality	
	γ_κ^{\min}	$\bar{\gamma}_\kappa$
Delaunay	0.18	0.966
MeshAdapt	0.36	0.972
Frontal	0.55	0.978

Table 1 Quality of the surface mesh using different planar mesh generators for the remeshing of the parametric space computed with the conformal map. The qualities we look at are the minimum aspect ratio γ_κ^{\min} and the mean aspect ratio $\bar{\gamma}_\kappa$.

4 Results

The numerical simulations aim at studying the effects of the mesh quality and the mesh algorithm on simulations results. The comparison of important clinical indicators (such as WSS) on different meshes shows how the mesh quality, and in particular whether accounting or not for the fluid boundary layer, affects the reliability of the simulations.

The blood flow simulations are performed with the open-source parallel finite element library LifeV³. The fluid problem is discretized in space using P1-P1 finite elements stabilized with the interior penalty technique described in [36] and discretized in time with an implicit Euler scheme. When considering compliant walls (FSI simulations), the wall structure is discretized in space with P1 finite elements and in time with a Newmark second order scheme. The FSI solver relies on a strongly coupled algorithm [5, 8, 6] where the coupling across the fluid-structure interface is satisfied exactly and the solution is not influenced by the added mass effect [12]. More details on the FSI solver can be found in [15].

Blood is modeled as a Newtonian fluid and if compliant vascular walls are considered, the wall structure is modeled as a linear elastic material.

³ <http://www.lifev.org>

4.1 Steady blood flow in a rigid aortic arch

We first study the steady blood flow in a patient specific aortic arch⁴ with rigid walls at low Reynolds $Re = 35$ (based on the inlet diameter and average inlet velocity)⁵. Two unstructured tetrahedral meshes of variable quality are considered: one obtained with the initial low-quality STL triangulation as input surface for the tetrahedral mesh generator and one with a remeshed surface as input. In order to obtain a very low quality mesh for the STL-based tetrahedral mesh, we disabled the mesh optimizations included in the tetrahedral mesh generator. For the remeshing of the lumen surface, we chose a uniform mesh size field. Both tetrahedral meshes have approximately $14k$ nodes. The quality histogram for those two tetrahedral meshes γ_τ is presented in figure 7.

As boundary conditions, we consider constant flux at the inlet [19], an homogeneous natural boundary condition at the outlets and a non-slip on the vessel walls. The Navier-Stokes equations are linearized by Fixed Point (FP) iterations. The linear system obtained by discretization of the linearized equations (Oseen problem) is solved by a GMRES iterative solver using a Krylov subspace of dimension 20 and an ILU(2) preconditioner.

Figure 8 shows the convergence of the residual of the linearized system at the 7th FP iteration. For the low quality mesh, we can see that the GMRES is unable to converge, the condition number of the matrix being rather high: $\kappa = 1.e^6$.

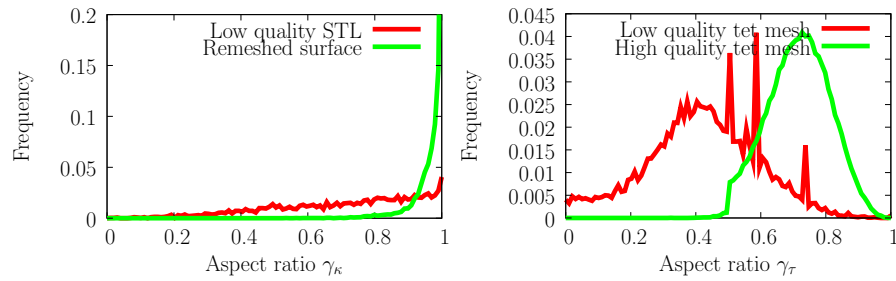


Fig. 7 Quality histogram γ_κ and γ_τ for the surface meshes and the tetrahedral meshes obtained respectively from the initial STL triangulation and the isotropic remeshed surface.

Fig. 8 Comparison of the convergence history obtained from simulation on the low and the high quality mesh.

⁴ The STL triangulation was found on the INRIA web site <http://www-roc.inria.fr/gamma/gamma/download>

⁵ Here we intend to test the effect of the mesh quality rather than reproduce physiological conditions

4.2 Unsteady blood flow in a rigid aortic arch

We study the unsteady blood flow in the same rigid aortic arch. We consider two different high quality tetrahedral meshes: one with a viscous boundary layer (such as depicted in yellow in Fig. 3) and one fully unstructured. Those two meshes have the same number of nodes (16k) and rely on a quality lumen surface triangulation that is obtained by remeshing the initial STL triangulation with a mesh size field h that is function of the vessel radius $R(\mathbf{x})$ (see Fig. 9b):

$$h(\mathbf{x}) = \frac{2\pi R(\mathbf{x})}{20}. \quad (11)$$

The vessel radius is evaluated in Gmsh as the Euclidian distance to the centerlines (see Fig. 9a) which are extracted with the open source VMTK library [3, 2].

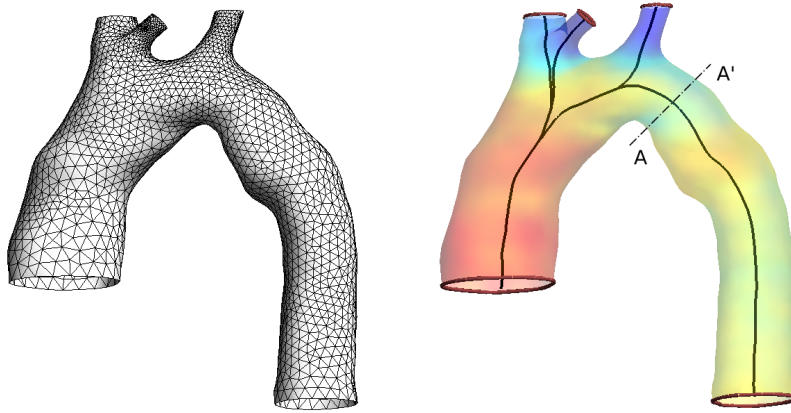


Fig. 9 Remeshed surface (Left) of the lumen of the aortic arch with a mesh size field h that is function of the vessel radius R . Right figure shows the computed centerlines (in black) and the distance of each surface point \mathbf{x} to the centerlines, i.e the vessel radius $R(\mathbf{x})$ (in color).

The blood flow simulation is conducted over a time-span of four cardiac cycles with a realistic time-dependent inlet blood flow rate. Unlike in the steady case, flux boundary conditions are prescribed [35] at the different outlets with a magnitude of respectively 15%, 10%, 10% and 65% of the inlet flow rate. We kept the same settings for the linear solver as in the steady case, except for the ILU preconditioner which was replaced by an algebraic multigrid preconditioner (implemented in LifeV as a wrapper to the ML package within the Trilinos library⁶). The coarse multigrid level was resolved with LU decomposition, and at the fine level Chebychev iterations were used as smoother.

⁶ <http://trilinos.sandia.gov>

We compare the shear vector forces at peak systole along the circumference at section AA' (see Fig. 9) computed on both meshes. The results obtained on the boundary layer mesh (Fig. 10) show higher value of the wall shear stress than on unstructured mesh. This is due to the fact that for the fully unstructured meshes, the mesh adjacent to the wall is not fine enough to resolve the boundary layer flow. This in turn leads to a diffused boundary layer and hence a lower velocity gradient and WSS value. To illustrate this, Fig. 11 shows a mesh convergence analysis of the mean WSS at this section for those two different types of meshes: (i) boundary layers meshes with 4 layers of uniform mesh size $h_{wall} = h_{BL}$ and filled with tetrahedra of mesh size $h_{center} = 10h_{BL}$, and (ii) fully unstructured meshes of size $h_{wall} = h_{center}$.

It is interesting to note that unlike the simulations of Sahni et al. [?, 41, 40] we did not observe any oscillatory distribution of WSS in the case of fully unstructured meshes (see the distribution of WSS in Fig. 10a). This is probably due to higher quality of the generated tetrahedral meshes.

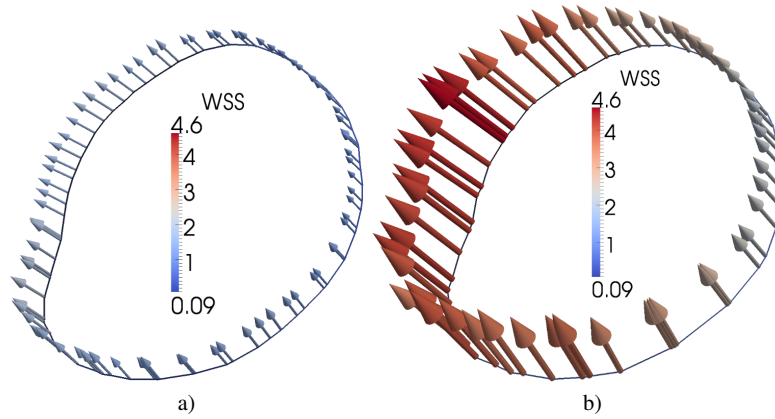


Fig. 10 Wall shear stress in $[dyn/cm^2]$ on the contour of the section A-A: mesh without (a) and with (b) boundary layer.

Fig. 11 Mesh convergence analysis for the mean WSS at peak systole along circumference AA' for boundary layer meshes and fully unstructured meshes of variable mesh size at the wall h_{wall} .

4.3 Unsteady blood flow in a compliant femoral bypass

For this test case, the geometric model of the distal anastomosis of a femoral bypass is obtained through a 3T MRI scanner of the left lower limb of a patient. The lumen geometry is subsequently reconstructed in 3D from the raw medical images using the open source software 3D slicer (see Fig. 12). The vascular wall is obtained by extruding the lumen surface in the outward normal direction with a given wall thickness of h of a tenth of the vessel radius. This extruded volume is then divided in 4 layers (see white volume in Figs. 12b and 12c).

For the meshing of the lumen volume (see red volume in Fig. 12b), we have considered different tetrahedral meshes: three fully unstructured meshes and three meshes with a viscous boundary layer. Those meshes are resumed in table 2.

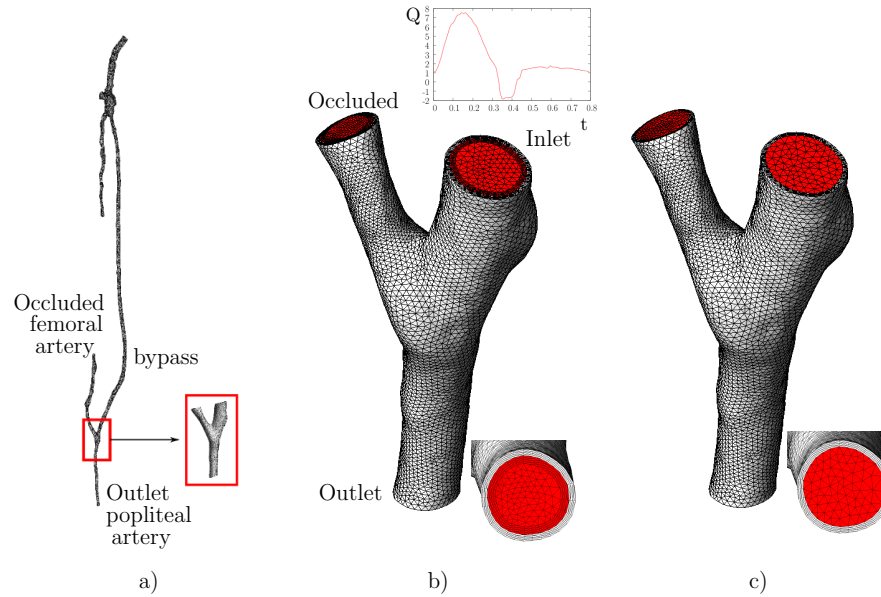


Fig. 12 Segmentation of the arteries of the left lower limb of a patient with a venous graft that bypasses the occluded femoral artery. We have focused on the geometry of the distal anastomosis. Two different type of meshes are considered for the lumen volume (in red): b) meshes with a viscous boundary layer (BL meshes) and c) fully unstructured tetrahedral meshes (U meshes). The mesh of the vascular wall is colored in white. The presented meshes are of middle mesh size (see Table 2).

The boundary conditions imposed at the inlet-outlet of the vessel are patient-specific measured fluxes (Fig. 12b), while an homogeneous Dirichlet condition is imposed on the occluded branch. The fluxes are imposed through a Lagrange

BL Mesh	Fine	Middle	Coarse
# Nodes	212.633	57.318	23.697
U Mesh	Fine	Middle	Coarse
# Nodes	154.732	36.490	8.508

Table 2 Different meshes considered for the numerical simulation: the boundary layer meshes (BL mesh) such as in Fig. 12b) and the fully unstructured meshes (U mesh) such as in Fig. 12c) with three different mesh sizes h_{center} : fine, middle and coarse. For the BL meshes, the ratio h_{center}/h_{wall} is taken to be 10.

multiplier as defective boundary conditions [19]. The Young modulus and Poisson coefficient characterizing the elastic material modeling the arterial wall are respectively $E = 4 \cdot 10^6 \text{ dyne/cm}^2$ and $\nu = 0.45$. The fluid dynamic viscosity is $\mu = 0.035 \text{ g/(cm s}^2)$. The densities for blood and arterial wall are respectively $\rho_f = 1 \text{ g/cm}^3$ and $\rho_s = 1.2 \text{ g/cm}^3$. Timings and validation for FSI solver used were already discussed in [16], while in [15] the scalability issue was addressed. The simulations reported in this work were run on the Cray XT6 supercomputer in the UK National Supercomputing Service HECToR⁷.

The FSI simulations are computationally expensive, so that they are run in parallel. As an example, the middle meshes are run on 48 cores, using 24 MPI processes per node and the simulation takes about 8 hours to run for one heartbeat. Due to the computational cost and since we are interested in the comparison of the WSS for the different meshes we did not run the simulation for several heartbeats, which would be necessary to reach periodicity and to obtain physiological results. We just ran for one heartbeat starting from a zero initial condition and we compared systolic hemodynamic values.

Fig. 13 shows the blood flow simulation results obtained with the boundary layer mesh of middle size. The streamlines show clearly the secondary flows which are in agreement with the WSS values. The flow impinging on the bed of the junction creates a region of high wall shear stress. Moreover, the blood flow is accelerated in the outlet popliteal artery since the graft is sewed on an artery of smaller diameter. This mismatch in diameter creates also a region of high wall shear stress near the outlet. The observed flow behavior in such an end-to-side bypass do not occur naturally in arteries and is widely implicated in the initiation of the disease formation processes [?, ?].

Figure 14 shows the WSS distribution at peak systole obtained for the six different meshes. WSS shows to be quantitatively better evaluated on the meshes with boundary layer, while even the finest mesh without boundary layer shows a substantial underestimation of the WSS with respect to all the the meshes with boundary layer.

⁷ <http://www.hector.ac.uk>

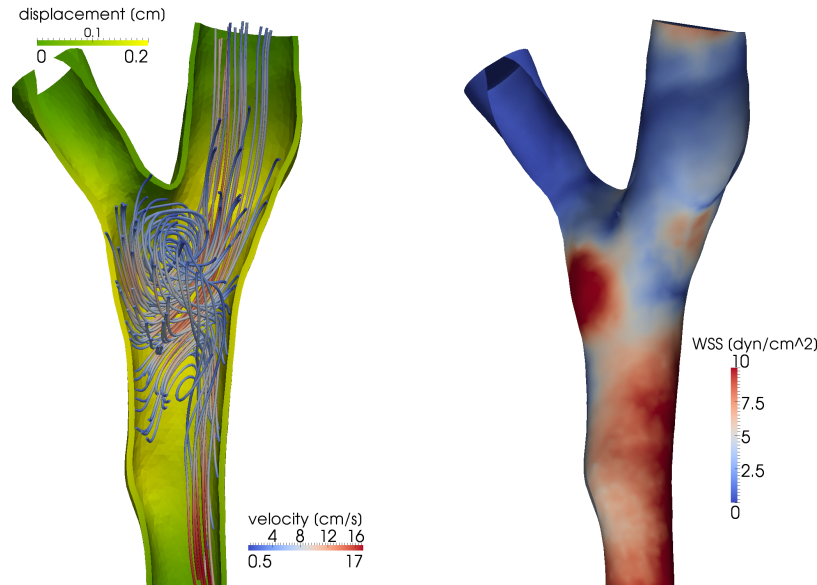


Fig. 13 Streamlines, wall displacement magnitude and distribution of WSS at end systole ($t = 0.3s$) obtained with the boundary layer mesh of middle mesh size.

5 Conclusion

We have presented a pipeline for generating spatially-adapted, high-quality tetrahedral meshes from a given STL triangulation and have shown its effectiveness for different cardiovascular simulations.

The presented algorithms include a remeshing strategy of an initial low-quality triangulation and an advancing front boundary layer generation technique. The remeshing strategy relies on the computation of a conformal mapping. We show that the remeshing in the parametric space is then optimal with a two-dimensional Frontal algorithm.

We have put to the fore the importance of the mesh quality and the mesh algorithm upon the simulations. By comparing important clinical indicators (such as WSS) on different meshes, we have shown how the mesh quality, and in particular whether accounting or not for the fluid boundary layer, affects the reliability of these evaluations.

Acknowledgements Swiss National Science Foundation under grant 200020-117587 and the European Research Council Advanced Grant "Mathcard, Mathematical Modelling and Simulation of the Cardiovascular System" Project ERC-2008-AdG 227058. The virtual pathological heart of the virtual physiological human (VPH2) project and the Swiss Platform for High-Performance and High-Productivity Computing (HP2C).

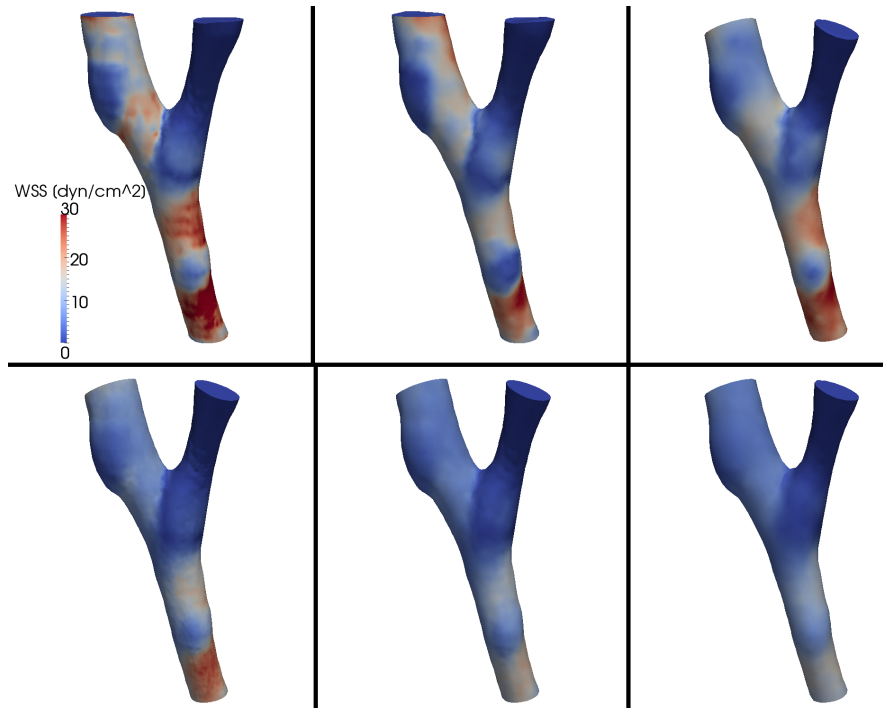


Fig. 14 Comparison of the WSS pattern for six meshes at peak systole ($t = 0.2s$). On the first row are the meshes with boundary layer, referring to table2, from left to right: FineBL, MiddleBL, CoarseBL. On the second row are the meshes without boundary layer. From left to right: Fine, Middle, Coarse.

References

1. Alliez, P., Meyer, M., Desbrun, M.: Interactive geometry remeshing. *Computer graphics (Proceedings of the SIGGRAPH 02)* pp. 347–354 (2002)
2. Antiga, L., Piccinelli, M., Botti, L., Ene-Iordache, B., Remuzzi, A., Steinman, D.: An image-based modeling framework for patient-specific computational hemodynamics. *Medical and Biological Engineering and Computing* **46**(11), 1097–1112 (2008)
3. Antiga, L., Steinman, D.: The vascular modeling toolkit <http://www.vmtk.org>
4. Babuska, I., Aziz, A.: On the angle condition in the finite element method. *SIAM Journal on Numerical Analysis* **13**, 214–226 (1976)
5. Badia, S., Quaini, A., Quarteroni, A.: Modular vs. non-modular preconditioners for fluid-structure systems with large added-mass effect. *Comput. Methods Appl. Mech. Engrg.* **197**(49-50), 4216–4232 (2008)
6. Barker, A.T., Cai, X.C.: Scalable parallel methods for monolithic coupling in fluid-structure interaction with application to blood flow modeling. *J. Comput. Phys.* **229**(3), 642–659 (2010). DOI <http://dx.doi.org/10.1016/j.jcp.2009.10.001>
7. Batdorf, M., Freitag, L., Ollivier-Gooch, C.: A computational study of the effect of unstructured mesh quality on solution efficiency. In: *Proc. 13th AIAA Computational Fluid Dynamics Conf.* (1997)

8. Bazilevs, Y., Gohean, J., Hughes, T., Moser, R., Zhang, Y.: Patient-specific isogeometric fluid-structure interaction analysis of thoracic aortic blood flow due to implantation of the Jarvik 2000 left ventricular assist device. *Computer Methods in Applied Mechanics and Engineering* **198**(45-46), 3534 – 3550 (2009). DOI DOI:10.1016/j.cma.2009.04.015. URL <http://www.sciencedirect.com/science/article/B6V29-4W99VW7-1/2/b5b7ebe43cedbd8a3b06caea7e6fa47b>
9. Bechet, E., Cuilliere, J.C., Trochu, F.: Generation of a finite element mesh from stereolithography (stl) files. *Computer-Aided Design* **34**(1), 1–17 (2002)
10. Borouchaki, H., Laug, P., George, P.: Parametric surface meshing using a combined advancing-front generalized delaunay approach. *International Journal for Numerical Methods in Engineering* **49**, 223–259 (2000)
11. Burleson, A., Turitto, V.: Identification of quantifiable hemodynamic factors in the assessment of cerebral aneurysm behavior. *Thromb Haemost* **76**(118-123) (1996)
12. Causin, P., Gerbeau, J.F., Nobile, F.: Added-mass effect in the design of partitioned algorithms for fluid-structure problems. *Comput. Methods Appl. Mech. Engrg.* **194**(42-44), 4506 – 4527 (2005). DOI DOI:10.1016/j.cma.2004.12.005
13. Compère, G., Remacle, J.F.: A mesh adaptation framework for large deformations. *International Journal for Numerical Methods in Engineering* (2009). Accepted
14. Connell, S., Braaten, M.: Semistructured mesh generation for three-dimensional navier-stokes calculations. *AIAA Journal* **33**(6), 1017–1024 (1995)
15. Crosetto, P., Deparis, S., Fourestey, G., Quarteroni, A.: Parallel Algorithms for Fluid-Structure Interaction Problems in Haemodynamics. MATHICSE technical report, Nr. 08.2010 Mai 2010 (2010)
16. Crosetto, P., Reymond, P., Deparis, S., Kontaxakis, D., Stergiopoulos, N., Quarteroni, A.: Fluid Structure Interaction Simulations of Physiological Blood Flow in the Aorta. Tech. rep. (2010)
17. Eck, M., DeRose, T., Duchamp, T., Hoppe, H., Lounsbery, M., Stuetzle, W.: Multiresolution analysis of arbitrary meshes. In: SIGGRAPH '95: Proceedings of the 22nd annual conference on Computer graphics and interactive techniques, pp. 173–182 (1995)
18. Floater, M.S.: Parametrization and smooth approximation of surface triangulations. *Computer aided geometric design* **14**(231-250) (1997)
19. Formaggia, L., Gerbeau, J., Nobile, F., Quarteroni, A.: Numerical treatment of defective boundary conditions for the navier-stokes equations. *SIAM J. Numer. Anal.* **40**, 376401 (2002)
20. Fried, I.: Condition of finite element matrices generated from nonuniform meshes. *AIAA Journal* **10**(219-221) (1972)
21. Garimella, R.V., Shephard, M.S.: Boundary layer mesh generation for viscous flow simulations. *International Journal for Numerical Methods in Engineering* **49**(1), 193–218 (2000)
22. George, P.L., Frey, P.: Mesh Generation. Hermes (2000)
23. Geuzaine, C., Remacle, J.F.: Gmsh: a three-dimensional finite element mesh generator with built-in pre- and post-processing facilities. *International Journal for Numerical Methods in Engineering* **79**(11), 1309–1331 (2009)
24. Gobin, Y., Counord, J., Flaud, P.: In vitro study of haemodynamics in a giant saccular aneurysm model: influence of flow dynamics in the parent vessel and effects of coil embolisation. *J. Neuroradiology* **36**, 530–536 (1994)
25. Graves, V., Strother, C., Partington CR, R.A.: Flow dynamics of lateral carotid artery aneurysms and their effects on coils and balloons: an experimental study in dogs. *AJNR Am J Neuroradiol* **13**(189-196) (1992)
26. Ito, Y., Nakahashi, K.: Direct surface triangulation using stereolithography data. *AIAA Journal* **40**(3), 490–496 (2002)
27. Kallinderis, Y., Khawaja, A., McMorris, H.: Hybrid prismatic/tetrahedral grid generation for complex geometries. *AIAA Paper* **34**, 93–0669 (1996)
28. Krams, R., Wentzel, J., Oomen, J., Vinke, R., Schuurbiens, J., de Feyter, P., Serruys, P., Slager, C.: Evaluation of endothelial shear stress and 3d geometry as factors determining the development of atherosclerosis and remodeling in human coronary arteries in vivo. *Arteriosclerosis, Thrombosis, and Vascular Biology* **17**, 2061–2065 (1997)

29. Kunert, G.: Anisotropic mesh construction and error estimation in the finite element method. *Numer. Methods Partial Differential Equations* **18**, 625–648 (2000)
30. Laug, P., Borouchaki, H.: Interpolating and meshing 3d surface grids. *International Journal for Numerical Methods in Engineering* **58**, 209–225 (2003)
31. Levy, B., Petitjean, S., Ray, N., Maillot, J.: Least squares conformal maps for automatic texture atlas generation. In: *Computer Graphics (Proceedings of SIGGRAPH 02)*, pp. 362 – 371 (2002)
32. Marchandise, E., Compère, G., Willemet, M., Bricteux, G., Geuzaine, C., Remacle, J.F.: Quality meshing based on stl triangulations for biomedical simulations. *International Journal for Numerical Methods in Biomedical Engineering* **83**, 876–889 (2010)
33. Marchandise, E., Carton de Wiart, C., Vos, W., Geuzaine, C., Remacle, J.F.: High quality surface remeshing using harmonic maps. Part II: Surfaces with high genus and of large aspect ratio. *International Journal for Numerical Methods in Engineering* p. accepted (2010)
34. Marcum, D.L.: Efficient generation of high-quality unstructured surface and volume grids. *Engrg. Comput.* **17**, 211–233 (2001)
35. Nicoud, F., Schoenfeld, T.: Integral boundary conditions for unsteady biomedical cfd applications. *Int. J. Numer. Meth. Fluids* **40**, 457465 (2002)
36. Nobile, F.: Numerical approximation of fluid- structure interaction problems with application to haemodynamics. Ph.D. thesis, Ecole Polytechnique Federale de Lausanne (2001)
37. Rebay, S.: Efficient unstructured mesh generation by means of delaunay triangulation and bowyer-watson algorithm. *Journal of Computational Physics* **106**, 25–138 (1993)
38. Remacle, J.F., Geuzaine, C., Compère, G., Marchandise, E.: High quality surface remeshing using harmonic maps. *International Journal for Numerical Methods in Engineering* **83**(403-425) (2010)
39. Remacle, J.F., Lambrechts, J., Seny, B., Marchandise, E.: Blossom-quad: a non-uniform quadrilateral mesh generator using a minimum cost perfect matching algorithm. *International Journal for Numerical Methods in Engineering* (submitted 2010)
40. Sahni, O., Jansen, K., Shephard, M.: Automated adaptive cardiovascular flow simulations. *Engineering with Computers* **25**(1), 25–36 (2009)
41. Sahni, O., Jansen, K.E., Shephard, M.S., Taylor, C.A., Beall, M.W.: Adaptive boundary layer meshing for viscous flow simulations. *Eng. with Comput.* **24**(3), 267–285 (2008)
42. Shaaban, A.M., Duerinckx, A.: Wall shear stress and early atherosclerosis. *American Journal of Roentgenology* **174**, 1657–1665 (2000)
43. Szczerba, D., McGregor, R., Szekely, G.: High quality surface mesh generation for multi-physics bio-medical simulations. In: *Computational Science – ICCS 2007*, vol. 4487, pp. 906–913. Springer Berlin (2007)
44. Tristano, J., Owen, S., Canann, S.: Advancing front surface mesh generation in parametric space using riemannian surface definition. In: *Proceedings of 7th International Meshing Roundtable*, pp. 429–455. Sandia National Laboratory (1998)
45. Wang, D., Hassan, O., Morgan, K., Weatheril, N.: Enhanced remeshing from stl files with applications to surface grid generation. *Commun. Numer. Meth. Engng* **23**, 227–239 (2007)
46. Zheng, Y., Weatherill, N., Hassan, O.: Topology abstraction of surface models for three-dimensional grid generation. *Engrg. Comput.* **17**(28-38) (2001)